Final report 2010-2012:

Current-induced domain wall motion in magnetic nanostrips

(CIDWM-nanostrips, PIEF-GA-2009-251887)

Jacob Torrejon*

Laboratoire de Physique des Solides, Université Paris-Sud,

CNRS UMR 8502, 91405 Orsay, France

(Dated: October 12, 2012)

I. SUMMARY

As a consequence of unexpected, pionneering and very interesting results showing a competition between Spin Transfer Torque (STT) and temperature gradients, that were obtained during the first year, we decided to modify the initial work plan for the second year, scheduled to be devoted to nanostrips with perpendicular anisotropy (Fig. 1). Therefore, we considered more interesting to investigate in details the role of thermal effects in the current-induced domain wall motion (CIDWM). Work with perpendicular anisotropy samples on spin-transfer torque was performed by other members of the group during that period, nevertheless.

Lately, the use and control of thermal effects in spintronic devices has attracted a lot of attention and opened up a new area of research called spin caloritronics[1]. Since the discovery of the Spin Seebeck effect[2], many works have investigated thermoelectric effects in magnetic metals[3–7] and even in insulating ferromagnets. This has forced considering other microscopic origins, like magnonic spin Seebeck effects[3,8,9]. This multitude of effects calls for experiments that weigh their relative magnitudes. Such an identification is especially important for nanosciences, as temperature gradients that are impossible in bulk samples are easily created in nanostructures.

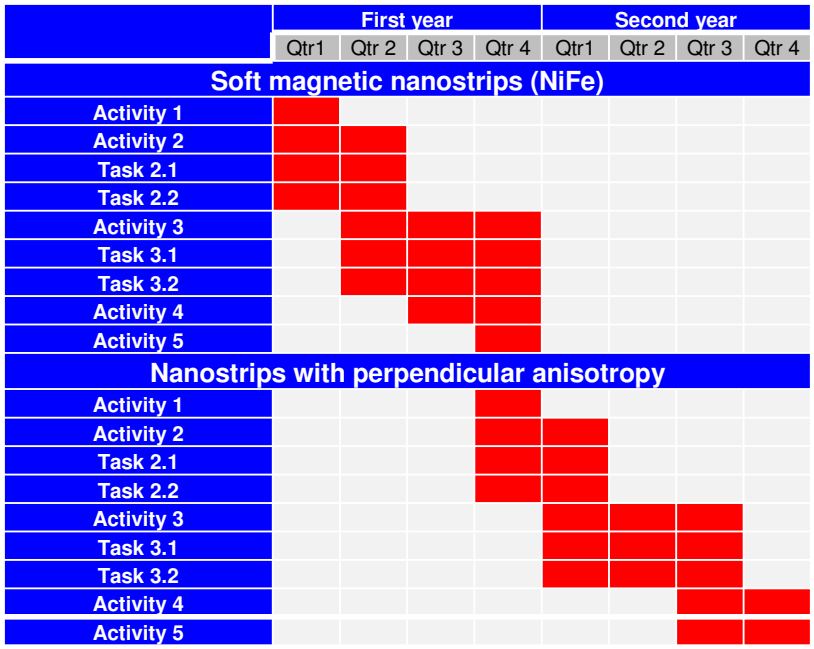

FIG. 1. Initial work plan proposed in the CIDWM-nanostrips project from september 2010 until august 2012.

Effects of sample heating, due to the large current densities required for observing DW displacement by STT, have been reported by many authors. The nucleation of domains[10–12] has been attributed to an increase of the sample temperature above the Curie temperature, whereas DW structure transformation and/or random displacement have been related to thermally activated Brownian motion of the wall position and magnetic moment[13,14]. The effect that I have discovered is qualitatively different, as a unidirectional DW displacement towards the hotter part of the nanostrip is observed, irrespective of the current direction. By tuning the heat dissipation in the samples and modeling the heat diffusion, we have concluded that this unidirectional motion can only be explained by the presence of a temperature profile along the nanostrip. A quantitative analysis of the experiments shows that, on top of the classical thermodynamic pressure on the domain wall, another force, probably the magnonic spin Seebeck effect, is displacing the domain walls.

Our original results were recently published in a high impact journal, **J. Torrejon, G. Malinowski, M. Pelloux, J. Curiale, R. Weil, A. Thiaville, D. Lacour, F. Montaigne and M. Hehn Phys. Rev. Lett. 109, 106601 (2012)**, and were disseminated in several international scientific events (the presenting person is underlined):

- A. Thiaville, J-Y Chauleau, J. Torrejon, J. Curiale, G. Malinowski, D. Lacour, F. Montaigne and M. Hehn. *Domain wall dynamics under short current pulses: spin transfer torque and others effects.* Physics of Magnetism 2011, invited talk, june 2011, Poznan (Poland).

- J. Torrejon, G. Malinowski, A. Thiaville, D. Lacour, F. Montaigne and M. Hehn. *Current induced domain wall motion in permalloy nanostrips.* The European School on Magnetism 2011, poster, august 2011, Targoviste (Romania).

- J. Torrejon, J. Curiale, G. Malinowski, A. Thiaville, D. Lacour, F. Montaigne and M. Hehn. *Concurrence entre transfer de spin et effects thermiques dans les nanopistes de permalloy.* XIV Colloque Louis Neel, oral presentation, september 2011, Brest (France).

- J. Torrejon and A. Thiaville. *Current-induced domain wall motion in magnetic nanostrips.* Marie Curie Researchers Symposium, poster, September 2011, Warsaw (Poland).

- J. Torrejon, J. Curiale, G. Malinowski, A. Thiaville, D. Lacour, F. Montaigne and M.

Hehn. *Joule heating effect as additional source of domain wall motion in NiFe nanostrips.* 56th MMM Conference, oral presentation, November 2011, Phoenix (USA).

- J. Torrejon, G. Malinowski, J. Curiale, M. Pelloux A. Thiaville, D. Lacour, F. Montaigne and M. Hehn. *Unidirectional thermal effects in domain wall motion.* ICM 2012, poster, july 2012, Busan (South Korea).

- J. Torrejon, G. Malinowski, A. Thiaville, J. Curiale, D. Lacour, F. Montaigne and M. Hehn. *Unidirectional thermal effects in current-induced domain wall motion.* Satellite conference Spin Dynamics in Nanomagnets, invited talk, july 2012, Seoul (South Korea).

- J. Torrejon, G. Malinowski, J. Curiale, M. Pelloux A. Thiaville, D. Lacour, F. Montaigne and M. Hehn. *Unidirectional thermal effects in domain wall motion: new architectures to test thermoelectric effects.* Seminar in National Institute for Materials Science (Tsukuba, Japan), July 2012.

In addition, more papers should be published with the further work described in the Perspectives section.

II. ACTIVITY 1: PREPARATION OF THE SAMPLE

Magnetically soft Ta(3 nm)/$Ni_{81}Fe_{19}$(17 nm)/Pt(3 nm) thin films were deposited onto Si substrates with or without a 100 nm SiO_2 layer, using UHV sputtering Fig. 2 (a). Nanopatterning was performed combining e-beam lithography, lift-off and etching, Fig. 2 (b). Nanostrips with a width varying between 200 and 500 nm and a length of 6 or 12 μm were obtained (see for more details my mid-term report).

III. ACTIVITY 2: CHARACTERIZATION OF THE SAMPLE

A. Structural characterization

The topography and morphology of the nanostrips were observed with SEM and AFM microscopy, Fig. 3 (a) and (b), respectively. We have designed two different samples: single and double curvature with 6 and 12 μm of length. The thickness and composition of each

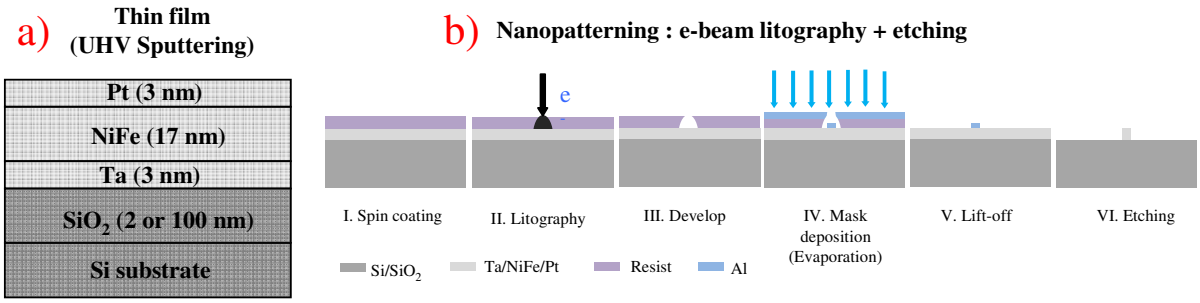

FIG. 2. General schemes of the (a) initial thin film deposited by UHV sputtering and (b) nanopatterning process of the nanostrip.

layer was verified with the Rutherford backscattering technique and chemical microanalysis by EDS (Energy-dispersive X-ray spectroscopy); see for more details my mid-term report.

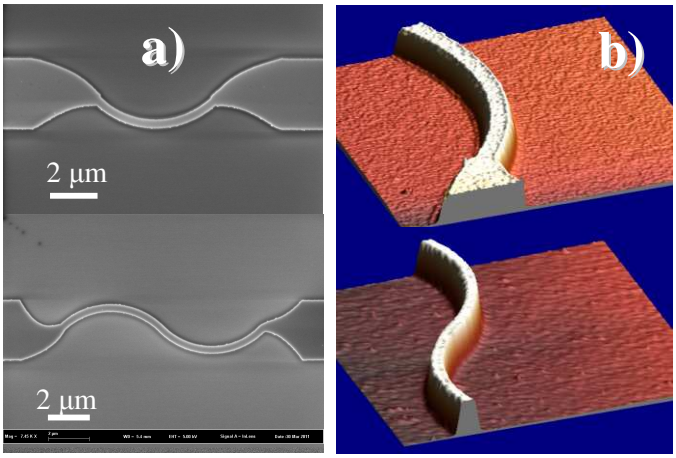

FIG. 3. (a) SEM and (b) AFM images of nanostrips with a width of 450 nm: (a) single curvature and (b) double curvature with a length of 6 and 12 μm, respectively.

B. Magnetic characterization

Basic magnetic characterization was firstly performed by static and dynamic techniques: SQUID, magneto-optical Kerr effect (MOKE, Fig. 4 (a) and (b)), and ferromagnetic resonance (FMR) techniques, Fig. 4 (c). From these measurements, we extracted the magnetic parameters of our permalloy samples: saturation magnetization M_s, remanence M_r, coercivity H_c and damping α (see for more details my mid-term report).

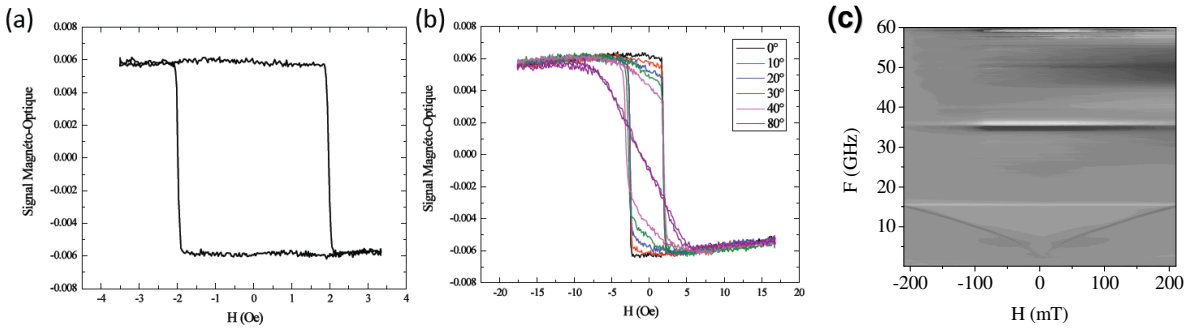

FIG. 4. Hysteresis loops measured by MOKE with the magnetic field applied along easy axis (a) and with angular variation in the same plane (b). FMR spectra as a function of frequency and magnetic field obtained by vector network analyzer FMR (c).

IV. ACTIVITY 3: STUDY OF CIDWM

The protocol of measurement is the following: first, a strong transverse field (80 kA/m) was applied, so that when it is removed an asymmetric transverse wall (ATW) is nucleated in the half point of the curvature, Fig. 5 (a). Note that samples with double curvature present head to head and tail to tail DW structures simultaneously, Fig. 5 (b).

The experimental setup used for the observation of DW structure and position before and after sharp current pulses (few nanoseconds of duration) combines high resolution MFM coupled to RF electronics. A one port configuration is adopted, where the Ti/Au coplanar waveguide (deposited in a second step by lithography and evaporation) is shorted with the nanostrip, Fig. 5 (c) (see for more details the mid-term report). The high frequency system comprises a picosecond pulse generator with risetime limitation of 55 ps, SMA adapters and cables, inverter (for changing polarity) and Picoprobe connectors.

For our nanostrip dimensions, the ATW is metastable and turns into the lower energy vortex wall (VW) with a large displacement, called automotion, after the first current pulse, Fig. 6. After that, MFM images are taken before and after current pulses in order to investigate the position, chirality and polarity of the VW.

Typical experimental results are illustrated by the MFM images of Fig. 7, obtained on double curvature samples with two DWs. For the sample grown on a Si substrate with a thick insulating silicon oxide layer (Fig. 7 a), the displacement of the DW towards the center of the nanostrip (red dash line) is distinctly easier compared to the motion towards

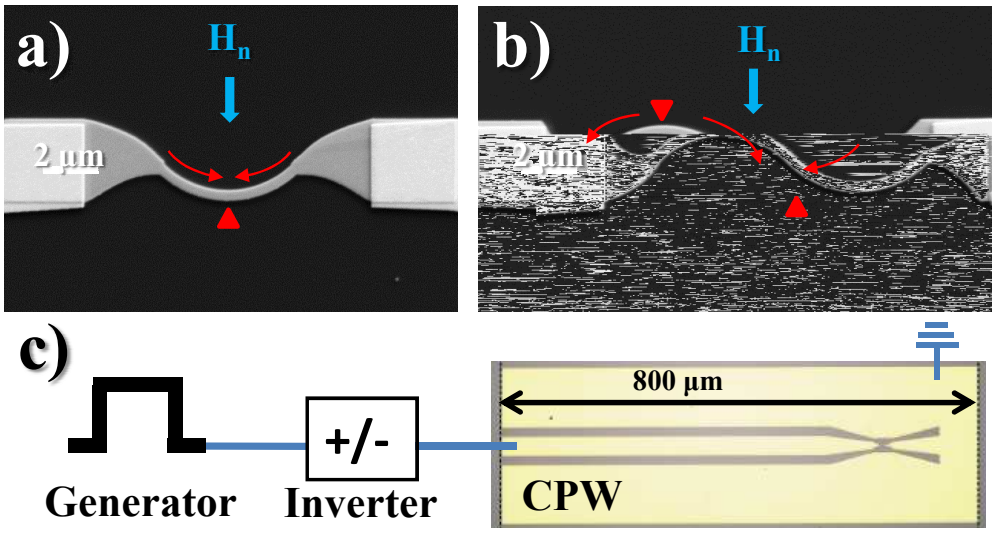

FIG. 5. Schematic of the experiment and sample structures. (a) SEM image of a single-curve sample, in which one DW is nucleated at the center by a transverse field H_n. (b) In the double-curve case, this procedure creates two DW at 1/4 and 3/4 of the length. (c) Optical image of the coplanar waveguide by which the sample is connected, with a schematic of the electronics.

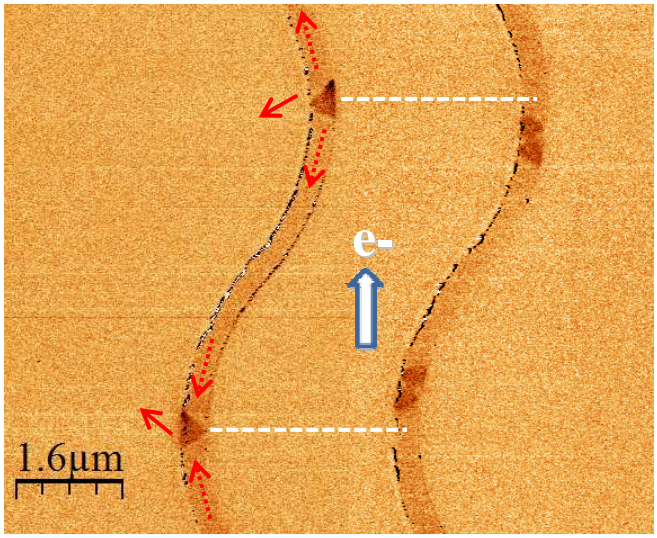

FIG. 6. Trasnformation from ATW to VW and automotion under one short current pulse.

the extremities. The experiments, repeated for the opposite DW magnetostatic charges (by changing the sense of the in-plane nucleation field), yield identical results, proving that no parasitic field compressing the central domain is present. An effect of a pinning site can be excluded since the initial DW position is different for each experiment. Indeed, the

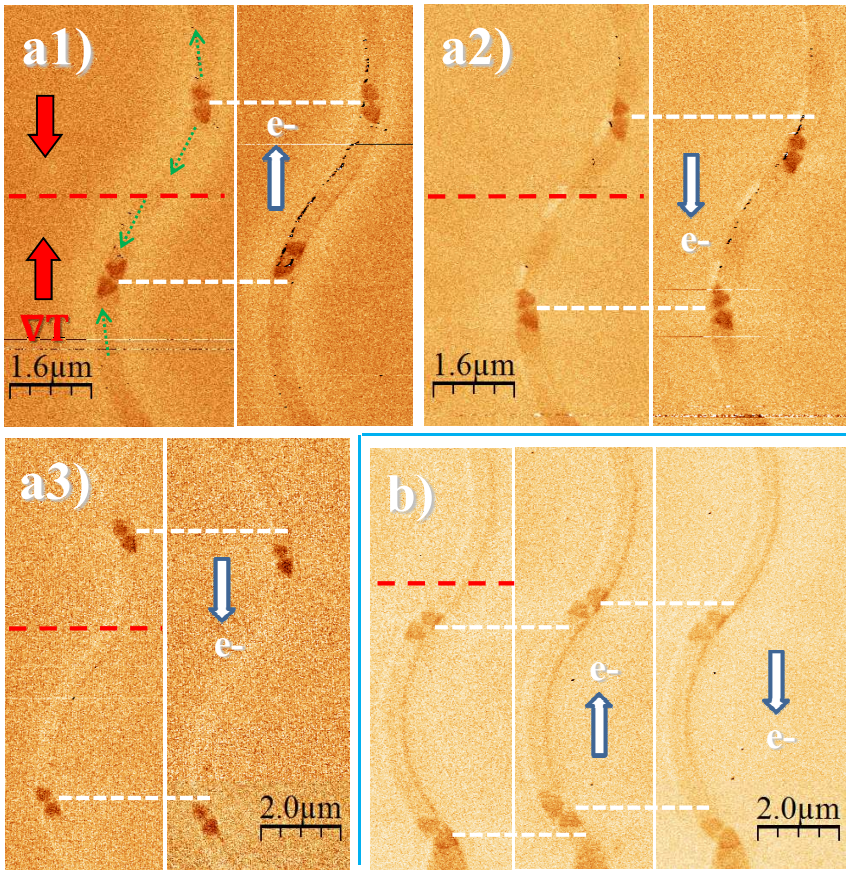

FIG. 7. VW motion observed by MFM in a nanostrip with double curvature, 450 nm wide and 12 μm long. The upper (lower) VW corresponds to the tail to tail (head to head) configuration (green arrows schematize the magnetization orientation). Current pulses of 2 ns duration and 3 TA/m^2 amplitude (open arrows display the electrons motion) are applied between consecutive MFM images. The temperature gradient, indicated by red full arrows, is towards the center (red dash line). Typical results for a nanostrip grown on a 100 nm oxide layer are shown in (a): (a1) electrons injected from bottom, motion of lower VW by 400 nm; (a2) electrons injected from the top, motion of upper VW by 800 nm; (a3) rarely observed motion of both VW, but still with a larger displacement towards the center. For an identical sample with native silicon oxide (b), symmetrical motion in both directions is observed (3 ns pulses).

nucleated DW is an (asymmetric) transverse wall[15], metastable in the present samples. On the first pulse, this DW transforms to the stable vortex wall (VW) structure, with an added displacement due to the automotion effect that shows some scatter[16]. The experiment was also reproduced on several samples, with identical or different nanostrip widths. In contrast

(Fig. 7 b), for an identical structure grown on Si substrate with only a native silicon oxide, no asymmetry is observed, in agreement with experiments on similar structures[16]: large and reproducible displacements of about 800 nm are observed (for 3 ns pulses).

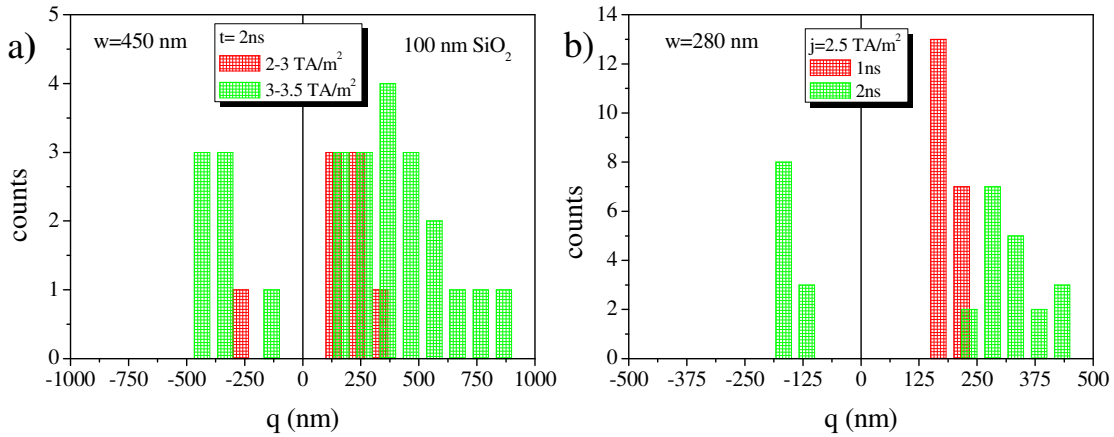

FIG. 8. Histogram of measured non-zero VW displacements, q, for two nanostrips with different width grown on thick silicon oxide: $w = 450$ (a) and $w = 280$ nm (b). Positive (negative) values correspond to the propagation towards the center of nanostrip (resp. ends). As there are 20 trials for each current pulse category and polarity, the number of no-motion results, not shown at $q = 0$, can be obtained by difference.

The difference between the two directions of motion, towards or away from the center, in the case of the thick oxide samples, was observed both on the motion probability and on the average displacement. In order to quantify the effect, the experiment was repeated many times in order to construct displacement histograms. Fig. 8 (a) shows typical results, obtained for a nanostrip with width $w = 450$ nm, for two current densities at constant 2 ns pulse duration. The total probability of motion is much higher when STT drives the DW towards the center part of the sample (62.5 %) compared to the opposite direction (20 %). Moreover, it is clear that the displacement is also much larger when the DW motion takes place toward the center of the nanostrip. The asymmetric distribution of DW displacements was observed for other nanostrip widths as well, provided that a thick oxide was present. As an example, Fig. 8 (b) shows the results obtained for a nanostrip with width $w = 280$ nm (for selected pulse durations at current density amplitude 2.5 TA/m^2). The total probability of motion, 97.5%, is much higher when STT drives the DW towards the center part of the sample, compared to 27.5% when the DW is driven away from the center. Moreover, it is

clear that the displacement is also much larger when the DW motion takes place toward the center of the nanostrip. As expected, DW motion probability and displacement increase as the pulse duration increases.

In comparison, histograms for the sample with only a native oxide are symmetrical: the DW propagation is very efficient (more than 75%) for both directions, towards center or to the ends. Fig. 9 shows typical measured histograms. They conform to what is expected for DW motion governed by STT.

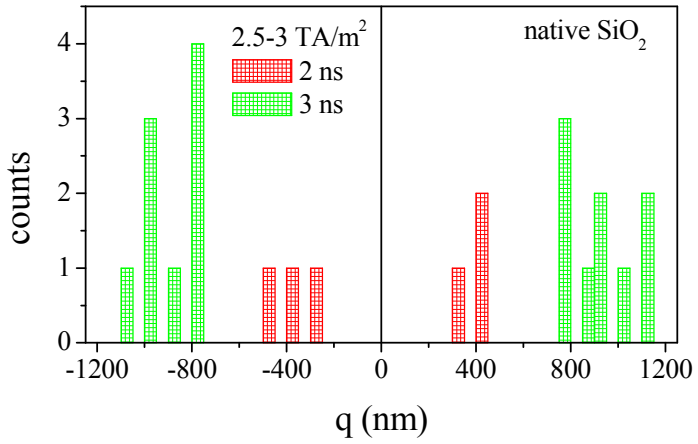

FIG. 9. Histograms of VW non-zero displacements, q, for a nanostrip with double curvature of width $w = 450$ nm in the native oxide case. Positive (negative) values correspond to the propagation towards the center of nanostrip (resp. ends). The total number of trials is 20 for 3 ns, but only 8 for the 2 ns pulses.

V. ACTIVITY 4: SIMULATION OF TEMPERATURE PROFILE BY FINITE ELEMENTS

A. 2D heat diffusion simulation: Joule heating

According to previous work, the temperature of the metallic nanostrip is mainly determined by the heat diffusion through the substrate[17]. In fact, the heat diffusion across the various layers of the substrate defines the time scales of the transient regimes.

We have first computed, using finite elements techniques (SAMCEF and COMSOL softwares), the temperature of the NiFe layer as a function of time, under constant current

flowing in the NiFe layer, Fig S10 (a). These calculations are performed in the 2D regime, i.e. for an infinite length of the NiFe nanostrip. The relevant material parameters are listed in Tab. I. Three regimes can be identified. The (linear) heating of the NiFe nanostrip, as if isolated, takes place only for $t \leq 0.1$ ns. The big difference between native and thicker SiO_2 is found in the intermediate regime. The insulating layer, with much lower thermal conductivity than Si and NiFe, induces a noticeable increase of the slope $\Delta T/\Delta t$. In addition, this regime extends up to about 50 ns, reaching very high temperatures around 1700 K for thicker oxide whereas, for the much thinner native oxide, this regime lasts only about 1 ns and induces a smaller temperature increase of 345 K. The third region, with the same small slope for both thicker and native SiO_2, corresponds to the heat diffusion through the much thicker Si; it extends up to the μs scale. Beyond this, the sample environment determines the temperature evolution. In our experimental setup, we work with very short pulse of few nanoseconds so that, for example, at 2 ns the temperature increases from 300 to 353 K with the native oxide and to 527 K with the thick oxide, as observed in Fig. 10 (a). A very similar behaviour is obtained for a single NiFe layer and the Ta/NiFe/Pt trilayer, with a small decrease of temperature (around 10 K for the sample with maximum SiO_2 thickness) in the case of the multilayer structure (not shown here). Experimentally, we have observed that DW structures disappear when the pulse length reaches values between 3 and 4 ns. For such times the nanostructure is heated close to the Curie temperature, 850 K, and the sample is uniformly remagnetized, in agreement with temperature values computed by the 2D simulation, Fig S10 (a).

TABLE I. Used physical parameters of NiFe, Si, SiO_2 and Au.

Material	Massic specific heat C_m (J kg^{-1} K^{-1})	Mass density ρ (10^3 kg m^{-3})	Thermal conductivity κ (W m^{-1} K^{-1})
NiFe	500	8.7	34.6
SiO_2	730	2.2	1
Si	700	2.34	149
Au	129	19.3	320

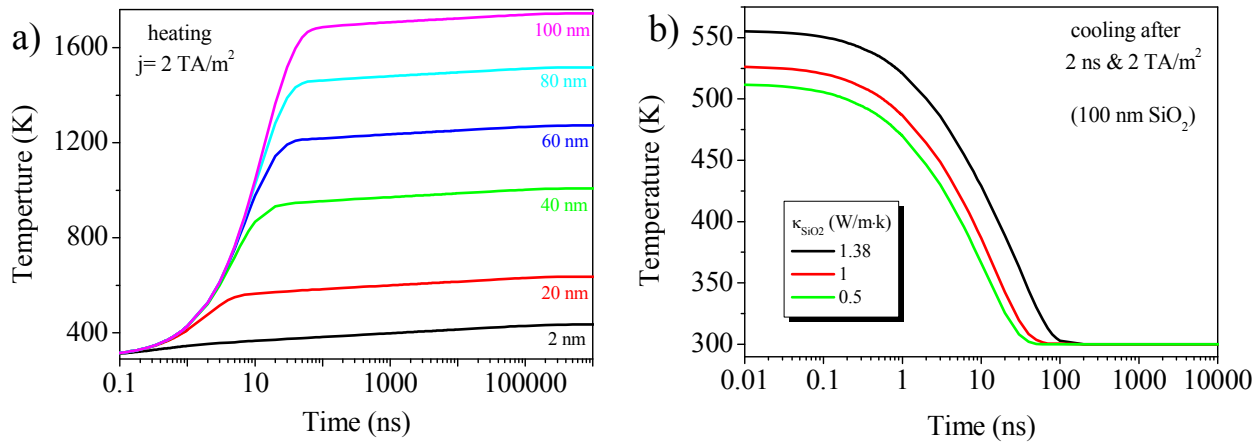

FIG. 10. 2D Calculation of the temperature transient regime as a function of time for NiFe nanostrips, 400 nm wide and 20 nm thick, with different thicknesses of SiO_2 (between 2 and 100 nm) at constant current density of 2 TA/m^2 (a). Evolution of temperature during cooling, after a 2 ns pulse for NiFe nanostrips with 100 nm thick SiO_2, for different values of the oxide thermal conductivity (b).

B. 2D heat diffusion simulation: cooling through the substrate

As this model considers an infinite length of the nanostrip, cooling occurs only through the SiO_2 substrate (Fig. 10 (b)). Apart from the SiO_2 thickness, the important role of thermal conductivity of SiO_2 during cooling can be observed in Fig. 10 (b). For 100 nm thickness, the cooling time is 40-100 ns. The initial temperature (the temperature at the end of the pulse) increases only slightly (from 500 to 550 K) for a lower value of thermal conductivity of the oxide.

C. 2D heat diffusion simulation: Perpendicular temperature gradient

The perpendicular temperature gradient has to be evaluated in order to quantify the anomalous Nernst effect. As shown in Fig. 11, the temperature profile is not linear (due to heat absorption only by the substrate, in the 2D case). Thus, there is no single value of the perpendicular temperature gradient. The values quoted in the text were evaluated in the vicinity of the interface. The temperature gradient decreases with increasing SiO_2 thickness, as the heat flow towards the substrate is decreased.

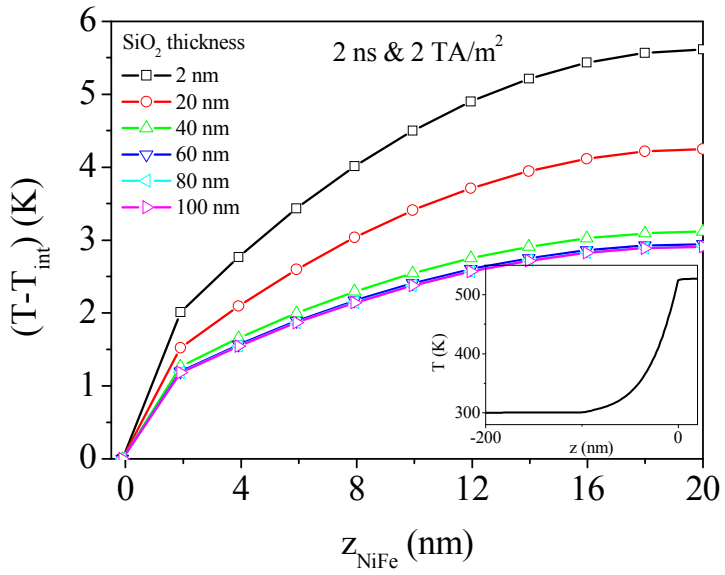

FIG. 11. Perpendicular temperature profile computed by 2D heat diffusion calculation, for different SiO_2 thickness at the end of a 2 ns current pulse with amplitude 2 TA/m^2. The inset shows the temperature profile within the top part of the substrate, for a 100 nm thick oxide.

D. 3D heat diffusion simulation: longitudinal temperature gradient

Finally, we consider a longitudinal temperature gradient. During the pulse, as it is extremely short, heat cannot diffuse out of the nanostrip. As a result, the temperature over the full length of the nanostrip is very homogeneous even at the end of the pulse (from the quoted value of the NiFe thermal conductivity[18] a heat diffusion constant $D \approx 8$ mm^2/s is estimated, leading to $\sqrt{Dt} \approx 100$ nm at $t = 1$ ns). On the other hand, the cooling lasts much longer, from a few ns (native oxide) to 50 ns (100 nm thick oxide), so that a non-uniform temperature profile can develop as a competition between heat absorption by the substrate and by the thick Au contacts at the nanostrip ends. The increased heat dissipation at the nanostrip ends leads to a larger temperature at the nanostrip center. In fact, the sample with thick oxide favors such a gradient, with a higher initial temperature and a much lower substrate heat conduction. The temperature profiles were evaluated with 3D time-dependent finite element modeling.

The results show that a 'temperature wave' sweeps the two halves of the nanostrip during cooling, Fig. 12 (a). These calculations, performed with tabulated parameters, give an order of magnitude of the longitudinal temperature gradient expected in such conditions. Large

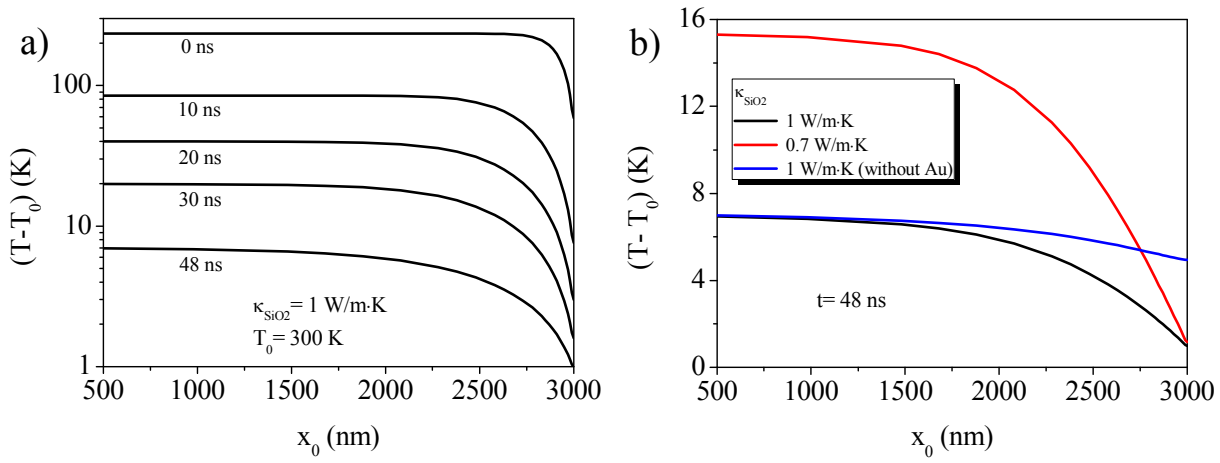

FIG. 12. Numerically calculated temperature profiles along one half of a 6 μm long straight nanostrip (400 nm wide and 20 nm thick), on top of a 100 nm silicon oxide, heated for 2 ns by a 2 TA/m^2 current density, as a function of time during the cooling phase (a). Temperature profiles at a cooling time of 48 ns for three different conditions: normal parameters ($\kappa_{SiO2} = 1$ W/m·K), minimun gradient (without Au contacts) and maximun gradient ($\kappa_{SiO2} = 0.7$ W/m·K) (b).

values above 100 K/μm are calculated initially and close to the nanostrip extremities whereas almost negligible values, less than 1 K/μm, are obtained at long times in the central part. The important role of the Au contact and κ_{SiO2} is explored in Fig. 12 (b) for different situations: nominal parameters, minimun gradient (without longitudinal heat diffusion) and maximun gradient (poor heat diffusion through the substrate).

VI. ACTIVITY 5: FORCES EXERTED BY A TEMPERATURE GRADIENT. DISCUSSION AND INTERPRETATION

Changing the substrate for the growth of the metallic multilayer has several consequences. The DW pinning is more important in the thick oxide case, with wider histograms and larger no-motion probability. However, this should not favor DW motion in any direction of the nanostrip. Another obvious consequence of a thick oxide is the reduced cooling by the substrate of the nanostrip submitted to Joule heating[19]. For example, we compute with a 2D calculation that after 2 ns with a current density of 2 TA/m^2, with 20 $\mu\Omega$.cm NiFe resistivity, the temperature in a 400×20 nm^2 nanostrip of infinite length has increased from

$T_0 = 300$ K to $T = 353$ K with a native 2 nm oxide, and up to 527 K for a 100 nm oxide. Thus, the Curie temperature is easily reached with a thick oxide, and indeed the nucleation of domains or a uniform remagnetization were observed for too intense or too long pulses. However, a uniform temperature increase over the entire length of the nanostrip does not by itself lead to an effective force on the DW. On the contrary, the weak variation of DW magnetostatic energy due to the finite nanostrip length, that pushes the DW out of the center, decreases at high temperature. Similarly, considering thermal activation, one only expects that an increased temperature favors DW motion down its magnetostatic potential well, thus towards the ends. Therefore, the only plausible explanation to account for our observations relies on the presence of a temperature gradient along the nanostrip.

A. Anomalous Nernst effect

As stressed recently, the largest gradient in such geometry is perpendicular to the film plane[20]. Numerical calculations for both a native oxide and a thick oxide layer of 100 nm give temperature gradients of $\partial T/\partial z = 340$ and 170 K/μm for a 2 ns, 2 TA/m^2 current pulse. Therefore, a larger gradient is present in the absence of oxide, reflecting only a better heat dissipation into the substrate, in qualitative contradiction with observations. Moreover, the thermoelectric effect that has been mentioned in such case[20,21] is the anomalous Nernst effect. A coefficient $\chi = 0.13$ between the anomalous and Seebeck effects has been recently measured in NiFe[18]. With the nominal NiFe resistivity, this corresponds to an induced in-plane current density of magnitude 2.7 GA/m^2, locally perpendicular to the magnetization. This magnitude is nearly 1000 times smaller than the injected current density, and moreover the STT from this Nernst current would have a zero average for a VW. As a result, the perpendicular temperature gradient cannot explain the observed effect.

B. Spin Seebeck effect

A spin transfer force due to the spin-dependent Seebeck effect has been considered recently[4,6,22,23]. Similarly to conventional STT induced by current, it involves a non-adiabatic β-like parameter, whose value is not well known. However, with the negative sign of the Seebeck coefficient of NiFe and a positive sign for β, this torque will push the

DW towards the cold part[23], opposite to our observations. In addition, the latter effect is relatively weak as one computes for a 100 K/μm gradient an equivalent charge current density of 10 GA/m^2 only (resistivity 20 $\mu\Omega$.cm, Seebeck coefficient -20 μV/K), more than 100 times smaller than the injected current density.

C. Classical thermodynamic pressure

A thermodynamic force, the gradient of DW energy caused by the temperature gradient, has been known for a long time[24]. As all magnetic energies disappear at the Curie temperature, it is expected to push the DW towards the hotter part[3], as observed here. In a mean-field model for the temperature dependence of magnetization, the DW energy in a soft material decreases linearly with temperature down to the Curie temperature. The exchange and shape anisotropy are both proportional to M_s^2, so that the wall energy as a function of wall position x can be expressed as follows

$$E = S\sigma_0 \frac{T_c - T_0 - x\frac{dT}{dx}}{T_c - T_0} \tag{1}$$

where S is the nanostrip cross-section, T_c the Curie temperature, T_0 the reference temperature (typically 300 K) and σ_0 the wall energy at the reference temperature. Such a linear dependence is identical to that realized under an applied magnetic field, $E = -2\mu_0 M_s H S x$. Therefore, the temperature gradient can be considered to induce an effective magnetic field favoring motion towards the hotter part

$$H_T = \frac{\sigma_0}{2\mu_0 M_s (T_c - T_0)} \frac{dT}{dx} \tag{2}$$

Taking tabulated values for permalloy, with T_c = 850 K and σ_0 =7.3 mJ/m^2 (from micromagnetic simulations), we compute a field H_T =6.5 A/m per 1 K/μm. Fig. 13 (a) displays the VW motion induced by an equivalent field of 650 A/m. The displacement obtained under a pure field corresponds surprisingly well with calculations for a uniform temperature gradient of 100 K/μm, as observed in Fig. 13 (b).

Assuming that the DW is not pinned and does not change structure, the DW displacement during the cooling phase is then simply[16] $q = (\gamma_0 \Delta_0/\alpha) \int H_T(t) dt$, where the value of

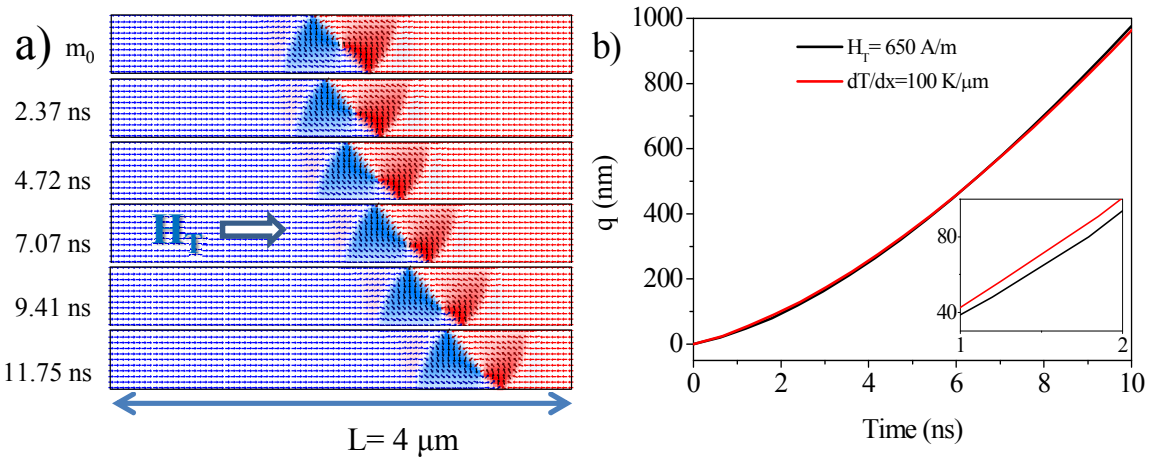

FIG. 13. Micromagnetic simulations of VW motion induced by equivalent field of 650 A/m. Initial and final position of VW for different times (a). VW motion versus time induced by the equivalent field, and by the temperature gradient (b).

the effective thermodynamic field has to be taken along the DW trajectory, γ_0 is the gyromagnetic ratio, Δ_0 the DW width and α the Gilbert damping constant of magnetization dynamics. From the computed 50 aJ DW energy and damping constant $\alpha = 0.01$, we expect a thermodynamic DW displacement of $q \approx 2000$ nm close to the ends of nanostrip, for a 2 TA/m^2, 2 ns pulse. In order to obtain a more precise evaluation of the DW displacement, taking into account STT, thermodynamic field and automotion effects, a numerical solution of the 1D model has been implemented. This model describes the VW dynamics by two conjugate coordinates, corresponding to the longitudinal position of the core (q) and the (generalized) DW magnetization angle (Φ), proportional here to the transversal position of the vortex core (y). It has been shown to properly depict the VW dynamics under current excitation[25]. The equations to be solved read

$$\begin{aligned} \frac{d\Phi}{dt} + \frac{\alpha}{\Delta_0}\frac{dq}{dt} &= \gamma_0 H_{\mathrm{T}} + \beta\frac{u}{\Delta_0}, \\ \frac{1}{\Delta_0}\frac{dq}{dt} - \alpha\frac{d\Phi}{dt} &= \gamma_0 H_K \sin\Phi\cos\Phi + \frac{u}{\Delta_0}. \end{aligned} \tag{3}$$

The effective thermodynamic field proportional to the local temperature gradient was given in Eq. (2), u is the velocity equivalent to the spin-polarized current density, H_K the

effective anisotropy field corresponding to the potential well that maintains the vortex core at the center of the nanostrip width. The assumed parameters were $M_s = 800$ kA/m, $\alpha = 0.01$, $\gamma_0 = 2.21\ 10^5$ m/(A·s), $\beta = 0.04$.

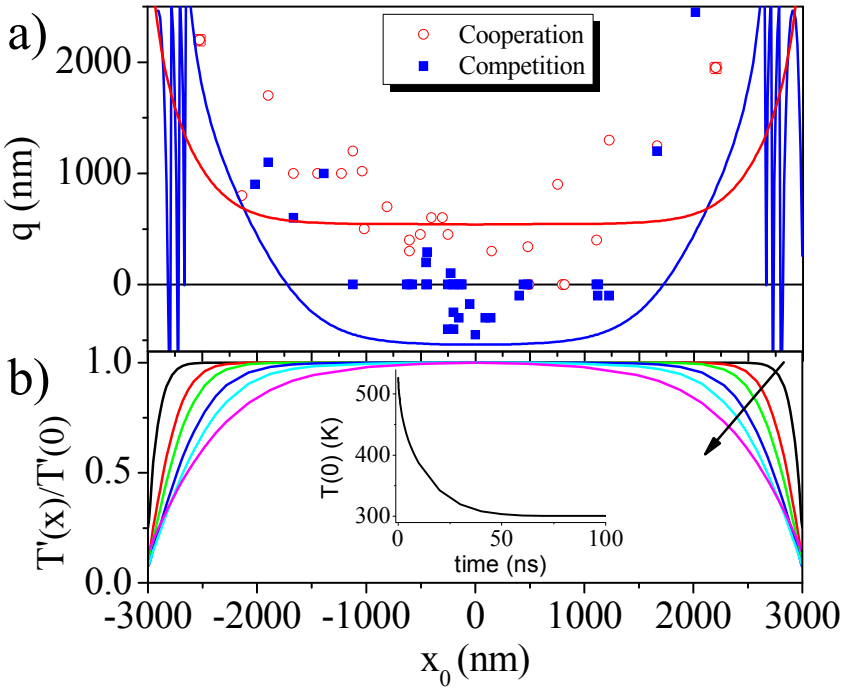

FIG. 14. (a) Measured VW displacement as a function of initial position (x_0), after injecting a current pulse, 2 ns long and with 2 TA/m^2 amplitude, for single curvature nanostrips 400 nm wide and 6 μm long. Positive displacement refers to motion towards the nanostrip center, and open (full) symbols correspond to STT driving the VW to the center (resp. end). The curves show the values calculated using a 1D model with 2 collective coordinates, including STT and the thermodynamic effective field, for a damping constant $\alpha = 0.01$. (b) Normalized temperature increase $T' = T - T_0$ profiles computed for times 0, 5, 10, 20, 30 and 48 ns after the current pulse end (arrow shows the effect of time increase). The decrease of central temperature $T(0,t)$ with time t is shown in inset.

The following parameters were extracted from the micromagnetic simulations: $\Delta_T = 24.2$ nm, $\mu_0 H_K = 44$ mT (corresponding to a core relaxation time of 14.3 ns), and $S\sigma_0 = 50$ aJ for a nanostrip with 400 nm wide and 17 nm thick. Ref. 26 provides charts for the variation of the main parameters of the 1D model for TW and VW as a function of nanostrip width and thickness for NiFe. Indeed, as the relaxation time of the VW structure is long (≈ 14 ns here), it is comparable to the cooling time of the nanostrip so that the VW

displacements induced by STT and thermodynamic effective field cannot be simply added. The results of such a calculation are superposed to the measurements in Fig. 14a.

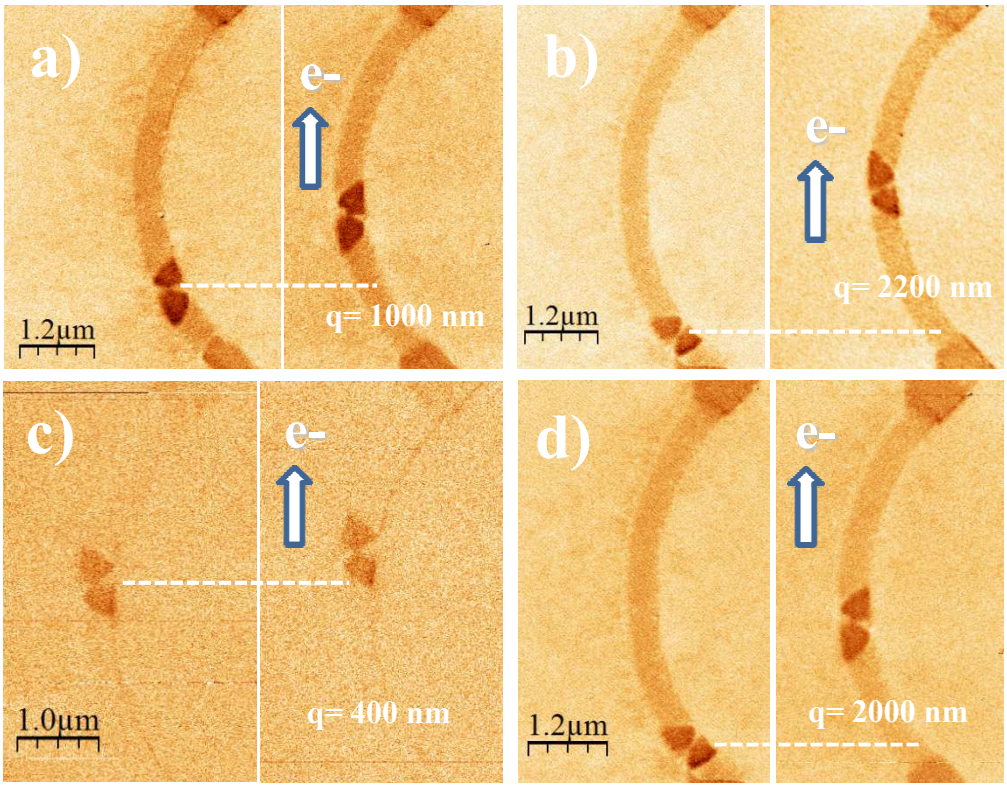

FIG. 15. VW displacement after current pulses (2 ns and 2-2.5 TA/m^2) observed by MFM in a single curvature nanostrip, 400 nm wide and 6 μm long, for different initial positions: at lower Au contact x_0 =-1750 nm (a), x_0 =-2600 nm (b), at the central region (c) and lower Au contact with change of chirality (d).

In a second series of experiments, the DW was deliberately placed at all positions along the nanostrip by means of an additional in-plane field. Note that, close to the nanostrip ends, VW structure transformations or even DW expulsion were sometimes observed, leading to a lower density of measured displacements. The calculations qualitatively reproduce the data, and also show VW transformation in the vicinity of the nanostrip ends, as seen by the large automotion linked to DW structure transformation[16].

Images coresponding to the data points shown in Fig. 14 (a) of the paper are provided. DW motion for an initial position close to the nanostrip end, mainly governed by the strong temperature gradient, shows very large displacement towards the center, Fig. 15 (a-b). Con-

versely, the spin transfer torque appears to be mainly responsible for the VW motion in the center of nanostrip, Fig. 15 (c). In addition, when the initial VW is close to the ends, a change of vortex chirality as shown in Fig. 15 (d), or the disappearance of the DW, are also observed. These phenomena are additional proofs of the very large torques applied to the VW at these positions. They correspond qualitatively to the changes of VW structure predicted by the $q - \Phi$ model, apparent in Fig. 14.

Thus, although full micromagnetic simulations are required for fully estimating the effects of such a temperature wave, we see that the combination of STT and thermodynamic DW motion explains the general trend of the data.

D. Magnons spin transfer: Magnonic Spin Seebeck effect

A significant difference however appears. Contrarily to the thermodynamic calculations, the DW were not observed to move freely under STT in the central part of the sample, especially in the case where motion due to STT and to the thermodynamic force are in competition. The reason for this prediction is clear from the normalized temperature profiles shown in Fig. 14 (b): even at 6 μm length there is virtually no temperature gradient in the vicinity (± 1 μm) of the nanostrip center, hence no thermodynamic effective field acting on the DW. Recent experiments have underlined the role of magnons in thermoelectric effects[8,9,27]. We note that the predictions about the direction of DW motion under magnon flow are of conflicting signs, either in the direction of the magnons flow[28], or towards the hot part of the sample[3,29,30], with no experimental proof up to now. Despite this, an interesting property of magnons is that they can transport information over micrometer-long distances, thus even in the absence of a local temperature gradient[3,8]. Therefore, it appears that the thermal effect observed on the DW motion close to the nanostrip center is likely to be explained by a magnonic spin Seebeck effect.

VII. PERSPECTIVES

A. 3D micromagnetic simulations taking into account thermal effects

The major limitation of the 1D model is not to take into account the domain wall width, comparable with the width of nanostrips. Therefore, full micromagnetic simulations are

required for fully understanding of thermal effects in CIDWM. As a first approximation, we consider the simple case of VW motion under constant temperature gradient, using the open software OOMMF. The temperature dependence is included in the micromagnetic parameters $A(T)$ and $M_s(T)$. We choose to keep a constant damping parameter α with temperature. We model a nanostrip of the size 4000 nm×500 nm×16 nm with a cubic cell size of 4 nm side.

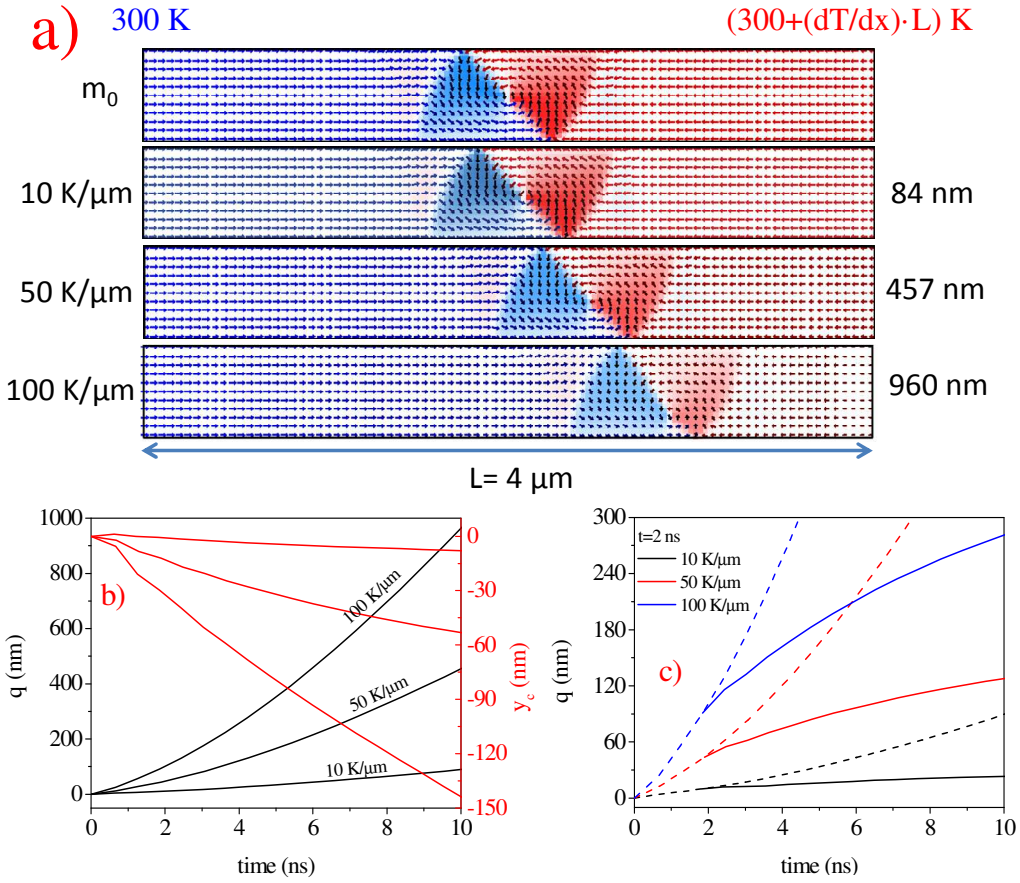

FIG. 16. Micromagnetic simulations of VW motion under dT/dx using LLG equation with parameters depending on T. (a) Initial and final position of VW at 10 ns for 3 different dT/dx=10, 50, 100 K/ m. (b) VW (black line) and core (red line) displacement versus time for different constant dT/dx. (c) VW motion versus time for temperature gradient applied for 2 ns.

Fig. 16 (a) shows the final position of VW at time 10 ns for three different constant longitudinal temperature gradients dT/dx = 10, 50, 100 K/μm, and the initial position (m_0). As we expect, the vortex wall displaces towards the hotter side, increasing with the

amplitude of dT/dx: 84, 457 and 946 nm for 10, 50 and 100 K/μm. The curves of motion as a function of time (Fig. 16 (b)) show the acceleration of the VW. The calculation for temperature pulses, Fig. 16 (c), shows that VW motion continues even when temperature gradient is switch off. During the temperature pulse, the vortex core displaces from the equilibrium position (in the center of the sample) to the border of nanostrip, as observed in Fig. 16 (a) (more clearly at higher temperature gradient) and (b) (red lines). This additional motion can be explained by the relaxation of the vortex core returning to the equilibrium. Similarly to VW motion by current pulse, we have like "thermal automotion regime". The displacement during automotion increases as the core vortex is farther from the center, that is, for larger amplitude of temperature gradient and times. Note that the total displacement extends over 20 ns, which is larger than typical characteristic time of relaxation.

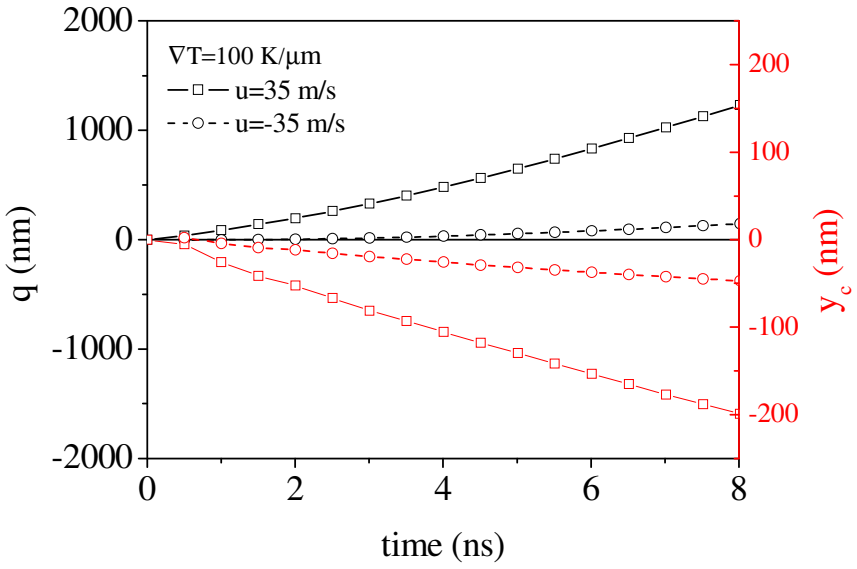

FIG. 17. Micromagnetic simulations of VW motion under dT/dx and STT using LLG equation with parameters depending on T. VW (black) and core (red) displacement versus time for constant $dT/dx = 100$ K/μm and $u = \pm 35$ m/s.

Fig. 17 shows simulation combining temperature gradient with STT. Larger (reduced) displacement are predicted when the themperature gradient is in cooperation (competition) with spin transfer torque, that is, when both point out in the same (antiparallel) direction. Moreover, the lateral displacement of the vortex core is larger for the cooperation case, which gives rise to longer relaxation time of the core.

For a more complex temperature gradient with time and spatial dependence, the home-

code developed in FORTRAN language will be more useful, although a powerul cluster is necessary. A poweful graphic card computer (GPU) was bought, which enables micromagnetic simulations 40 times faster than previously. As a starting point, we will investigate two situations: a) VW motion induced by spin-polarizad current and spatially-dependent temperature gradient with parameters $M(T(x))$ and $A(T(x))$, to evaluate the classical thermodynamic effect and b) VW motion under constant temperature, then constant parameters M_0 and A_0, induced by space-dependent thermal field, $H_{th}(T(x))$, in order to get more informaction about magnonic spin Seebeck effect. The action of the magnons can be separated from the thermodynamic aspects in simulations where the temperature is constant in the part of the system which contains the DW, whereas magnons are injected from a distant, hotter region.

B. Analysis of time-resolved VW motion, induced by current and temperature gradient, using XMCD-PEEM technique

Simulations have shown that the temperature gradient in our nanostrip is time-dependent. Indeed, at the end of the 2 ns pulse, the temperature in the nanostrip is uniform and the appearance of a temperature gradient results from a competition between heat flow within the contact pads and the substrate. As a consequence, the VW submitted to spin transfer torque during the pulse duration might move in the direction of the electrons flow and, on a longer timescale, the VW might come back to a position close to the center under the action of forces related to the presence of the temperature gradient, Fig. 18.

Since MFM is a very slow technique, only static VW imaging could be performed before and after the current pulse. Recently, we have submitted a proposal to the SOLEIL synchrotron for the next year. The aim of this project is to unravel the dynamics of VW submitted to varying charge and heat currents. To do so, we will use stroboscopic time-resolved XMCD-PEEM which has already been successfully used on the TEMPO branchline[31]. The direct observation of the VW displacement in real time is essential to understand all the phenomena governing VW dynamics submitted to a pulsed current. The time-resolved XMCD-PEEM experiment will allow direct imaging of reproducible domain wall displacement. Of particular interest is the motion of the domain wall occurring during the heat dissipation. This experiment will provide crucial information on the strength of the thermal

force acting on the domain wall and on how the domain wall reacts in presence of such a temperature gradient.

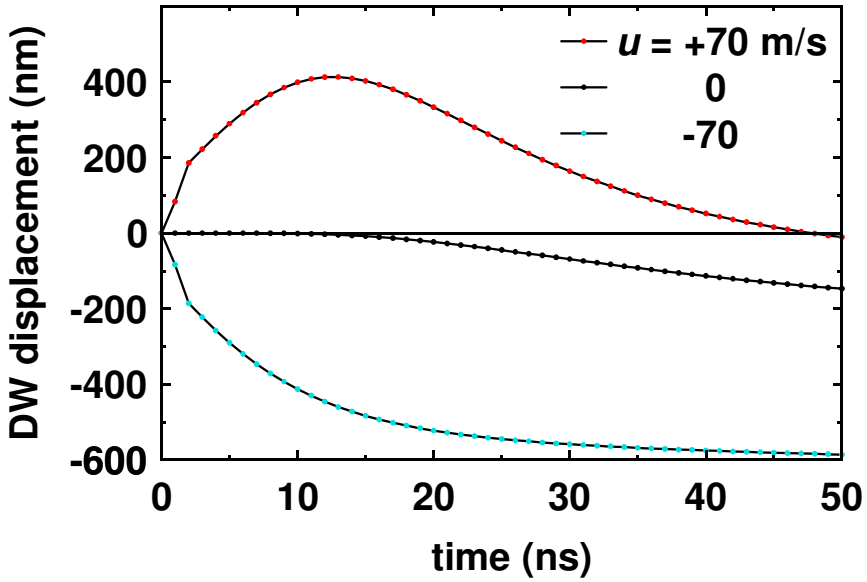

FIG. 18. Temporal profiles of VW displacemet computed with 1D micromagnetic model, injecting a current pulse, 2 ns long and with $u = \pm 70$ m/s amplitude, for single curvature nanostrips 400 nm wide and 6 μm long. Initial position $x_0 = 1850$ nm and $\alpha = 0.02$.

C. DW dynamics under nonlocal spin-transfer torque

It has been predicted that current driven wall motion is, in the steady velocity regime, adequately described by an effective nonlocal nonadiabatic parameter[32]. This parameter has been found to be 20% larger than its local counterpart for a vortex wall in a NiFe nanostrip and hardly modified for a transverse wall, Fig. 19, for reasonable electron diffusion parameters. This may account for the yet unexplained experimental evidence that vortex walls move more easily under current when compared with transverse walls. It is related to the presence in the DW structure of significant magnetization gradients over the electron transport characteristic lengthscales.

We have fabricated a set of nanostrips with particular dimensions (width and thickness) where ATW and VW present the same energy, that is for $w \times t \approx 1500$ nm^2 (250×6, 300×5, 400×4 and 500×3 nm^2). The main objective will be to investigate the nonlocal-STT in

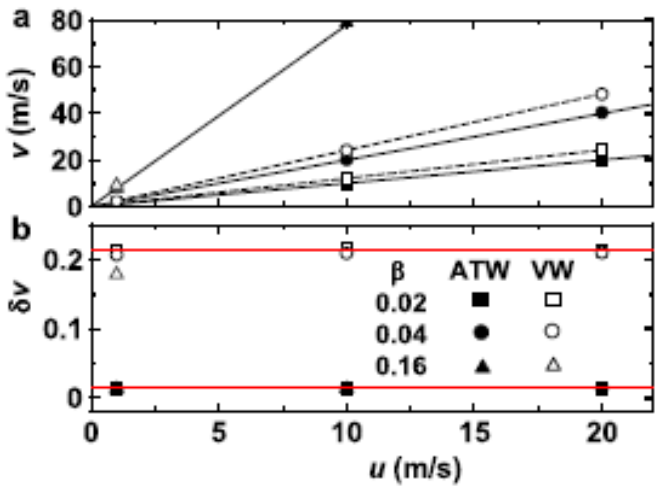

FIG. 19. Numerically computed steady-state DW velocities v as a function of u and for different values of β, for the ATW (filled symbols) and the VW (open symbols)[32].

VW and ATW and to probe experimentally that the firsts are more mobile. To do so, we will use MFM coupled to high frequency setup and eventually time-resolved XMCD-PEEM.

---

* torrejon@lps.u-psud.fr

[1] G.E.W Bauer, E. Saitoh, and B.J. van Wees, Nature Mater. **11**, 391 (2012).

[2] K. Uchida, S. Takahashi, K. Harii, J. Ieda, W. Koshibae, K. Ando, S. Maekawa, and E. Saitoh, Nature **455**, 778 (2008).

[3] D. Hinzke and U. Nowak, Phys. Rev. Lett. **107**, 027205 (2011).

[4] A.A. Kovalev and Y. Tserkovnyak, Phys. Rev. B **80**, 100408(R) (2009).

[5] K.M.D. Hals, A. Brataas, and G.E.W. Bauer, Solid State Commun. **150**, 461 (2010).

[6] Z. Yuan, S. Wang, and K. Xia, Solid State Commun. **150**, 548 (2010).

[7] G.E.W Bauer, A.H. MacDonald, and S. Maekawa, Solid State Commun. **150**, 459 (2010).

[8] J. Xiao, G.E.W. Bauer, K.C. Uchida, E. Saitoh, and S. Maekawa, Phys. Rev. B **81**, 214418 (2010).

[9] J.C. Slonczewski, Phys. Rev. B **82**, 054403 (2010).

[10] A. Yamaguchi, S. Nasu, H. Tanigawa, T. Ono, K. Miyake, K. Mibu, and T. Shinjo, Appl. Phys. Lett. **86**, 012511 (2005).

[11] Y. Togawa, T. Kimura, K. Harada, T. Akashi, T. Matsuda, A. Tonomura, and Y. Otani, Jpn. J. Appl. Phys. **45**, L683 (2006).

[12] M. Cormier, A. Mougin, J. Ferré, A. Thiaville, N. Charpentier, F. Piéchon, R. Weil, V. Baltz, and B. Rodmacq, Phys. Rev. B **81**, 024407 (2010).

[13] M. Laufenberg, W. Bührer, D. Bedau, P.-E. Melchy, M. Kläui, L. Vila, G. Faini, C.A.F. Vaz, J.A.C. Bland, and U. Rüdiger, Phys. Rev. Lett. **97**, 046602 (2006).

[14] F. Junginger, M. Kläui, D. Backes, U. Rüdiger, T. Kasama, R.E. Dunin-Borkowski, L.J. Heyderman, C.A.F. Vaz, and J.A.C. Bland, Appl. Phys. Lett. **90**, 132506 (2007).

[15] M. Kläui, C.A.F. Vaz, J.A.C. Bland, L.J. Heyderman, F. Nolting, A. Pavlovska, E. Bauer, S. Cherifi, S. Heun, and A. Locatelli, Appl. Phys. Lett. **85**, 5637 (2004).

[16] J.-Y. Chauleau, R. Weil, A. Thiaville, and J. Miltat, Phys. Rev. B **82**, 214414 (2010).

[17] J. Curiale, A. Lemaître, G. Faini, and V. Jeudy, Appl. Phys. Lett. **97**, 243505 (2010).

[18] A. Slachter, F.L. Bakker, and B.J. van Wees, Phys. Rev. B **84**, 020412(R) (2011).

[19] C.-Y. You and S.-S. Ha, Appl. Phys. Lett. **91**, 022507 (2007).

[20] S.Y. Huang, W.G. Wang, S.F. Lee, J. Kwo, and C.L. Chien, Phys. Rev. Lett. **107**, 216604 (2011).

[21] S.U. Jen and L. Berger, J. Appl. Phys. **59**, 1285 (1986).

[22] M. Hatami, G.E.W. Bauer, Q. Zhang, and P.J. Kelly, Phys. Rev. Lett. **99**, 066603 (2007).

[23] G.E.W. Bauer, S. Bretzel, A. Brataas, and Y. Tserkovnyak, Phys. Rev. B **81**, 024427 (2010).

[24] A. Thiele, A. Bobeck, E. Della Torre, and U. Gianola, Bell Syst. Tech. J. **50**, 711 (1971).

[25] L. Thomas, M. Hayashi, X. Jiang, R. Moriya, C. Rettner, and S.S.P. Parkin, Nature **443**, 197 (2006).

[26] A. Thiaville, Y. Nakatani, F. Piéchon, J. Miltat, and T. Ono, Eur. Phys. J. B **60**, 15 (2007).

[27] Y. Kajiwara, K. Harii, S. Takahashi, J. Ohe, K. Uchida, M. Mizuguchi, H. Umezawa, H. Kawai, K. Ando, K. Takanashi, S. Maekawa, and E. Saitoh, Nature **464**, 262 (2010).

[28] D.-S. Han, S.-K. Kim, J.-Y. Lee, S.J. Hermsdoerfer, H. Schultheiss, B. Leven, and B. Hillebrands, Appl. Phys. Lett. **94**, 112502 (2009).

[29] A.V. Mikhailov and A.I. Yaremchuk, JETP Lett. **39**, 354 (1984).

[30] P. Yan, X.S. Wang, and X.R. Wang, Phys. Rev. Lett. **107**, 177207 (2011).

[31] J. Vogel, M. Bonfim, N. Rougemaille, I.M. Miron, S. Auffret, B. Rodmacq, G. Gaudin, J.C. Cezar, F. Sirotti, and S. Pizzini, Phys. Rev. Lett. **108**, 247202 (2012).

[32] D. Claudio-Gonzalez, A. Thiaville, and J. Miltat, Phys. Rev. Lett. **108**, 227208 (2012).